ADVANCED MATERIALS TECHNOLOGIES
www.advmattechnol.de

A Self-Powered and Efficient Triboelectric Dehydrator for Separating Water-in-Oil Emulsions with Ultrahigh Moisture Content

Fangming Li, Xingfu Wan, Jiaju Hong, Xinyang Guo, Minzheng Sun, Haijia Lv, Hao Wang, Jianchun Mi, Jia Cheng, Xinxiang Pan, Minyi Xu, and Zhong Lin Wang**

Oil–water emulsions are a considerable hazard to the environment, ecology, and human health, if not appropriately treated. This study proposes a self-powered and efficient triboelectric dehydrator (TED) based on a wind-driven freestanding rotary triboelectric nanogenerator (FR-TENG) to separate water-in-oil emulsions. This TED can form a high-voltage electric field in the emulsion when the FR-TENG is driven by mechanical energy. The dehydration performance of the TED is analyzed in detail through multiphysics-coupled models and experiments. It is found that the TED can dehydrate water-in-oil emulsions with a wide range of initial moisture contents. In particular, even when the initial moisture content is 60%, which is near the phase inversion concentration of the emulsion, the dehydration rate of the TED can still reach 99.41%. In addition, the performance of TED is demonstrated in a simulated situation of wind, suggesting that the present TED has great potential application for separating oil–water emulsions by harvesting environmental energy.

F. Li, X. Wan, J. Hong, X. Guo, M. Sun, H. Lv, H. Wang, J. Mi, X. Pan, M. Xu
Dalian Key Lab of Marine Micro/Nano Energy and Self-powered Systems
Marine Engineering College
Dalian Maritime University
Dalian 116026, China
E-mail: xuminyi@dlmu.edu.cn

J. Mi
College of Engineering
Peking University
Beijing 100871, China

J. Cheng
State Key Laboratory of Tribology
Department of Mechanical Engineering
Tsinghua University
Beijing 100084, China

X. Pan
School of Electronics and Information Technology
Guangdong Ocean University
Zhanjiang 524088, China

Z. L. Wang
Beijing Institute of Nanoenergy and Nanosystems
Chinese Academy of Sciences
Beijing 101400, P. R. China
E-mail: zlwang@binn.cas.cn

Z. L. Wang
School of Materials Science and Engineering
Georgia Institute of Technology
Atlanta, GA 30332-0245, USA

The ORCID identification number(s) for the author(s) of this article can be found under https://doi.org/10.1002/admt.202200198.

DOI: 10.1002/admt.202200198

1. Introduction

Oil–water emulsions generated by oil production and other human activities are extremely harmful to the environment,[1,2] ecology,[3,4] and human health,[5] if they are not appropriately treated. Several oil–water separation technologies exist to treat these oil–water emulsions, such as physical separation methods, chemical demulsification, and electric dehydration. Physical separation methods such as gravity settling are mainly utilized for the initial separation of the oil–water mixture. They are usually energy intensive and require considerable power consumption.[6–10] Chemical demulsification relies on chemical agents to destroy the interfacial stability of oil–water emulsions, thus achieving oil–water separation. It is widely used in many applications but could generate impurities and cause secondary pollution.[11–13] Electric dehydration has the advantages of high dehydration efficiency and quality, but it can only work at low moisture content with a complex power supply.[14–16] Overall, a large amount of energy or chemicals is consumed during oil–water treatment. Therefore, it is highly desired to develop a sustainable and efficient method for separating oil–water emulsions.

A triboelectric nanogenerator (TENG) can instantly convert environmental energy into electricity and then serves as an energy harvester, active sensor portable power sources, and self-powered systems.[17–23] Relying on the electrostatic induction effect, TENGs can generate an extremely high electric field, and their open-circuit voltage (V_{OC}) can easily reach a few thousand volts.[24] This makes the TENG a high-voltage power supply driven by environmental energy for water disinfection,[25] sterilization,[26] microplasma generation,[27] soft robots,[28,29] microfluidics,[30,31] cell printing technology,[32] and electrostatic spinning.[33] In particular, Lei et al.[34] developed a TENG with a charge-accumulation strategy to provide a sustained ultrahigh output voltage of 20 kV, which was used to trigger continuous electrophoresis and dielectrophoresis in the oil, resulting in a self-powered oil purification system. Previous studies[35–38] found that traditional electric dehydrators cannot function well beyond a moisture content of 20% due to water chain caused short-circuit current (I_{SC}) damage. However, the short-current output of TENGs is usually at

the level of microamps due to the finite transferred charge of TENGs.[24] The high-voltage and low-current properties of a TENG could expand the applicable moisture content range in electric dehydration. The above works suggest that a TENG has great potential to serve as a high-voltage source driven by environmental energy for the electric dehydration of water-in-oil emulsions.

In the present work, a self-powered and efficient triboelectric dehydrator (TED) is proposed, consisting of a pair of electrodes that connect to a freestanding rotary TENG (FR-TENG). When environmental energy such as wind energy is used to drive the TENG, it provides a high-voltage electric field to the emulsion. A multiphysics-coupled model is established to study the dynamic performance of water droplets in oil under the high-voltage electric field. Through both simulations and experiments, the dehydration performance of the TED is analyzed in detail. The present experimental results show that the dehydration rate reaches 99.41% even when the initial moisture content is 60%. Above this moisture content, the water-in-oil emulsions will transform into the oil-in-water emulsion. In addition, the TED driven by wind energy is successfully demonstrated to dehydrate the water-in-oil emulsions. The present work proves that TED has great potential for separating oil–water emulsions.

2. Results and Discussion

2.1. Structure and Working Principle of TED

Figure 1a demonstrates a schematic diagram of the wind-driven TED network for crude oil treatment. As shown in Figure 1b, a TED is driven by offshore wind energy by connecting to a windmill. The wind-driven TED unit floats on the sea with the buoyancy block. Through pipelines, multiple wind-driven TED units distributed in neighboring water areas are deployed in a TED network. The pipeline transfers crude oil from the platform to TED units, and the dehydrated liquids are returned to the platform separately through the oil and water outlets. Due to the applicable moisture content limit of conventional electric dehydrators, crude oil treatment on offshore platforms usually uses electrical dehydration as the last stage of treatment, before which the emulsion moisture content is reduced to a suitable range by other methods. The wind-driven TED network simplifies the dehydration process and saves energy, thus releasing space and improving production efficiency.

Figure 1c illustrates the TED structure, consisting of an FR-TENG connecting to a dehydrator. The design of an FR-TENG enables the polyvinyl chloride (PVC) film on the rotor soft to contact with the nylon film on the stator. Compared with other

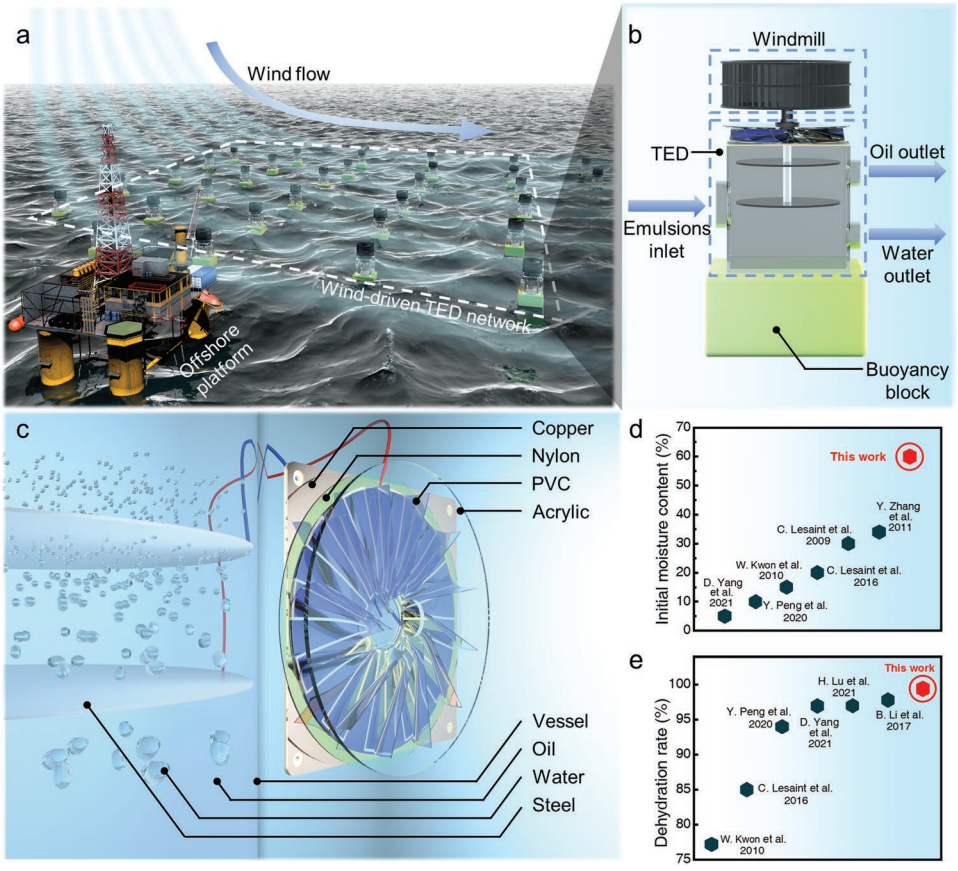

Figure 1. Design and application of TED for separating water-in-oil emulsions. a) The wind-driven TED network for crude oil treatment. b) Structure diagram of a wind-driven TED unit. c) Schematic of TED. Comparison of d) the initial moisture content and e) final dehydration rate obtained in this work with others.[14,39–45]

tightly frictional TENGs, the FR-TENG has less resistance torque between the rotor and the stator. Therefore, it is easier to harvest environmental energy, such as wave energy, wind energy, and ocean current energy. By connecting the FR-TENG directly with the two electrodes of the electric dehydrator, an electric field is built in the vessel. According to electro-hydrodynamics, the electric field provided by the FR-TENG produces dielectric force to the water-in-oil emulsion. With the effect of the dielectric force, the oil-wrapped water droplets produce deformation, oscillation, and coalescence. As a result, the dehydration is accelerated significantly.

Oil–water emulsions are sorted into water-in-oil emulsions and oil-in-water emulsions with different moisture contents. The oil phase is continuous in water-in-oil emulsions, while the aqueous phase is discrete, and the phase continuity in the oil-in-water emulsion is the opposite. When the moisture content increases and exceeds the phase inversion concentration, the water-in-oil emulsion turns into the oil-in-water emulsion.[39–41] It is well known that oil is usually a good insulator. Water is insulated in the ideal situation, but in practice, it is conductive. The conductive continuous aqueous phase between two electrodes could cause the destruction of the electric field.

The TED works well at 60% moisture content, at which the moisture content is close to phase inversion concentration. As shown in Figure 1d, the applicable moisture content of the TED is far beyond that in the literature.[14,42–45] It is because of water chains that occur continuously in the traditional dehydrator,[36–38] which causes short-circuit current damage. In contrast, the short-circuit current damage does not happen in TED. Since the FR-TENG is a high-voltage, low-current power source, the TED is barely influenced by the water chain, which is a great advantage over traditional electric dehydration equipment.

Additionally, as shown in Figure 1e, to the best of our knowledge, TED is more efficient compared with other works.[14,42,45–48] The final dehydration rate is 99.41% for the TED, at 60% initial moisture content, 1000 V cm^{-1} average electric field intensity, parallel electrode, and 50 °C. In summary, the dehydrating performance of the TED is outstanding for ultrahigh moisture content water-in-oil emulsions.

2.2. The Output and Characteristics of an FR-TENG

To further analyze the characteristics of TED, the output and characteristics of the FR-TENG are tested. As shown in **Figure 2**a, the gap distance between the rotor and the stator determines the contact area of the PVC film and the nylon film when the same set of PVC films is used. On this basis, the gap distance influences the output of the FR-TENG. Additionally, the speed of rotation also affects the output.

The V_{OC} and I_{SC} are measured by the circuit shown in Figure 2b. Results are shown in Figure 2c,d, measured at a 5 mm gap distance and rotational speed from 20 to 400 rpm. The V_{OC} increases with the rotational speed of the rotor. At 20 rpm, the V_{OC} reaches 1.6 kV and up to a maximum of 3.0 kV at 400 rpm. The speed change affects the I_{SC} more obviously, rising from 14.7 μA at 20 rpm to a maximum of 193.7 μA at 400 rpm.

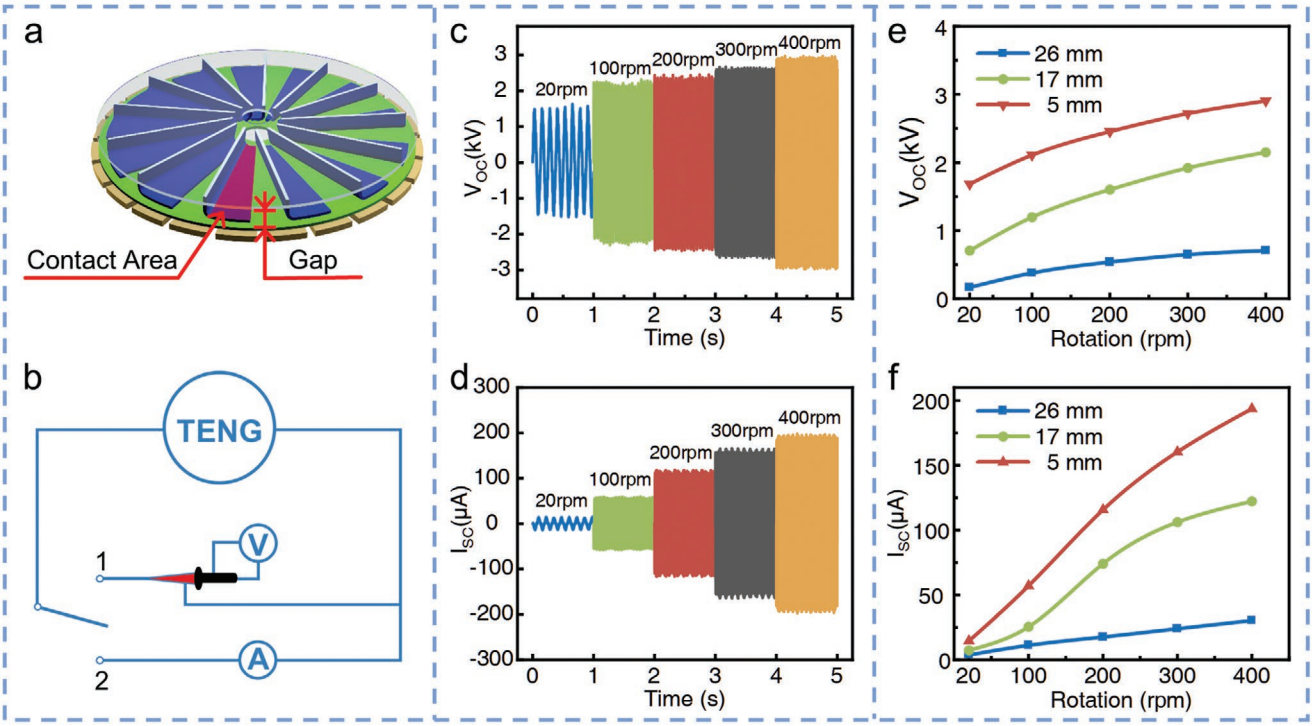

Figure 2. Structure and electric characteristics of the FR-TENG. a) Structure diagram of the FR-TENG. b) Circuit schematic measuring electric characteristics of the FR-TENG. Switching positions 1 and 2 mean the measurement of open-circuit voltage and short-circuit current of the FR-TENG, respectively. c) Open-circuit voltage and d) short-circuit current of the FR-TENG with various rotational speeds. e) Open-circuit voltage and f) short-circuit current of the FR-TENG with various gap distances.

The peak values of V_{OC} and I_{SC} at different rotational speeds for the FR-TENG with various gap distances are shown in Figure 2e,f. The contact area is reduced by increasing the gap distance, leading to a lower output. V_{OC} covers from 200 to 2000 V at these three gap distances. Despite the variation in frequency, the frequency within this range has a negligible effect on the dehydration efficiency.[49] It allows experiments to be executed at different electric intensities. These experiments also demonstrate that smaller TENGs can drive dehydration. These provide the foundation for designing a TED according to various energy harvesting methods.

2.3. Dehydration Performance of the TED

2.3.1. Dynamic Performance of Water Droplet in Oil under a High-Voltage Electric Field

Figure 3a shows the charge transfer during a full cycle containing four stages. The nylon and PVC are charged by frictional contact. Positive charges on 12 pieces of PVC films induce corresponding negative charges on electrodes of the FR-TENG directly below the contact area. The FR-TENG is connected directly to the electrodes in the emulsion. As the rotor rotates, charges are transported from the electrodes of the FR-TENG to the electrodes of the dehydrator, thus generating an electric field force on the water-in-oil emulsion. The electric field force is mainly produced around water droplets, while its magnitude is positively related to the strength of the electric field. By continuously repeating this cycle, the water droplets keep getting deformed, oscillated, and coalescenced, which significantly increases the dehydration speed.

According to electro-hydrodynamics theory, the emulsion satisfies the Navier–Stokes equations[50]

$$\rho\frac{\partial u}{\partial t}+\rho\left(u\cdot\nabla u\right)=\nabla\cdot\left[-pI+\mu\left(\nabla u+\left(\nabla u\right)^{T}\right)\right]+\rho g+F_{st}+F_{e} \quad (1)$$

$$\nabla\cdot u=0 \quad (2)$$

where ρ is the fluid density, p is the pressure, μ is the fluid viscosity, and u is the fluid velocity. The additional terms F_{st} and F_{e} are the interfacial force and the electric force, respectively. The interfacial force is the resistance, and the electric force is the driving force of the coalescence. The interfacial force is defined as follow

$$F_{st}=\nabla\cdot\left[\gamma\left(I-\left(nn^{T}\right)\right)\delta\right] \quad (3)$$

Here, I and T are the identity matrix and the transposed matrix, $\gamma$is the surface tension, n is the interface normal, and δ is the Dirac delta function that is zero except at the fluid interface. The fluid is subjected to forces in the electric field, as shown in the following equation[51]

$$F_{e}=q_{e}\,E-\frac{1}{2}E^{2}\nabla\varepsilon+\frac{1}{2}\nabla\left[E^{2}\rho\left(\frac{\partial\varepsilon}{\partial\rho}\right)_{T}\right] \quad (4)$$

where q_e is the charge density, E is the electric field, ε is the fluid permittivity, and T is the temperature. The three terms in the equation represent the Coulomb force, the dielectric force,

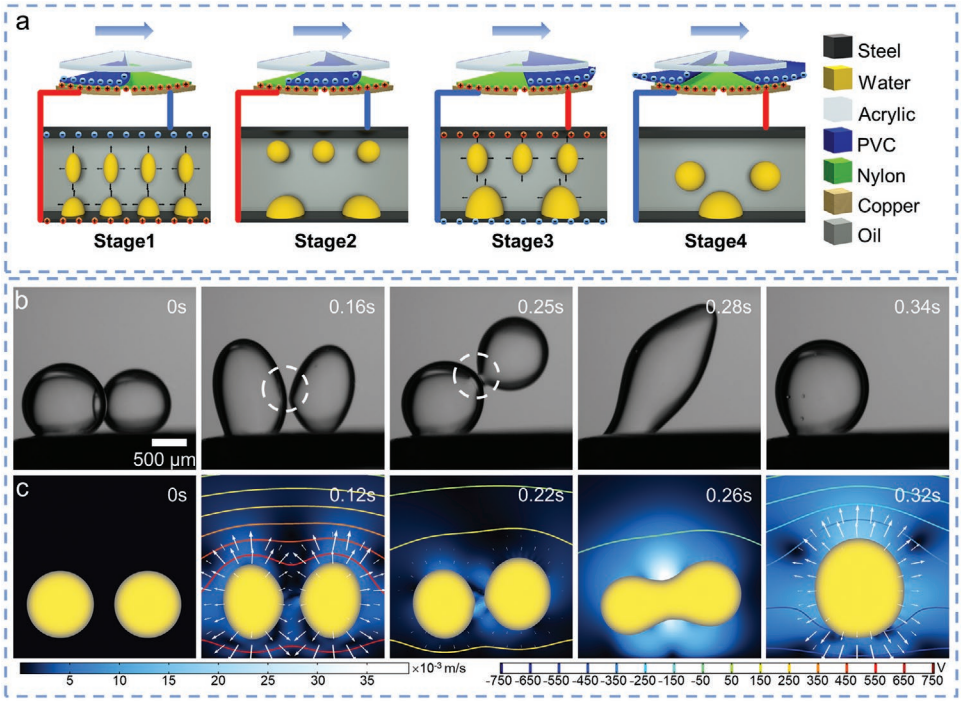

Figure 3. Dynamics of water droplets in emulsions under high-voltage electric field built by an FR-TENG. a) Four stages in one full cycle of the TED. The b) experiment and c) simulation for the coalescence of water droplets directly driven by the FR-TENG.

and the electrostriction force, respectively. Although a small amount of charge is transferred from the two electrodes to the water-in-oil emulsion, its quantity is almost negligible.[52] The electrostriction force is neglected since the emulsion is considered an incompressible fluid. Therefore, the dominating force on the water-in-oil emulsion in the electric field is the dielectric force

$$F_e \approx -\frac{1}{2}E^2\nabla\varepsilon \tag{5}$$

Equation (5) indicates that the emulsion is subjected to an electric field mainly induced by the inhomogeneity of the dielectric constant. In electro-hydrodynamics theory, it can be calculated equivalently by the Maxwell stress tensor. The detailed deduction is presented in Note S1 (Supporting Information).

The electric coalescence of water droplets is divided into oscillation coalescence and dipole coalescence. They are analyzed in detail through both simulations and experiments. In the simulation and experiment, the droplet size is enlarged to 500 μm, and the parallel electrode distance is reduced to 5 mm to observe the dynamic processes intuitively. The lowest accessible rotation speed of the FR-TENG for the experiment is 20 rpm. Correspondingly, in the simulation, the top and bottom electrodes' voltage waveforms are tuned to 4 Hz, and the peak voltage is set to 1.5 kV. A multiphysics model is developed in COMSOL to perform this simulation. The model consists of three physical field models, including a laminar flow model to calculate the flow of the emulsion, a level-set two-phase flow model to track the changes at the oil–water interface, and an electrostatic model to estimate the electric field changes in the water-in-oil emulsion. The three models are fully coupled to simulate the interactions between the emulsion and the electric field.

Figure S1 (Supporting Information) shows the deformation of a water droplet in the simulation and experiment. It is the basis of oscillation coalescence and dipole coalescence. The arrows in the simulation indicate the magnitude and direction of the electric field force. It should be noted that the arrow lengths in Figures S1 and S2 (Supporting Information) are proportional, and the scale factors are 3E-4 and 5E-5, respectively, while the arrow length in Figure 3c is logarithmic, the range quotient is 500, and the scale factor is 10E-6. It can be observed that as the electric potential increases, the upward dielectric force increases. In the experiment, water droplets were successfully deformed by the dielectric force generated by the FR-TENG. The dynamic process of the water droplet deformation driven by the FR-TENG is shown in Video S1 (Supporting Information).

In practice, as shown in Figure S2 (Supporting Information), the dielectric forces generated above and below the water droplet are not in the same magnitude, making the water droplet deform and oscillate simultaneously, which is because the electric field around the water droplet varies with its location owing to the inhomogeneity of the electric field. The oscillation of water droplets increases the opportunity of water droplets collision, which forms the basis of the oscillation coalescence. The process of the oscillation is shown in Video S2 (Supporting Information).

The simulation and experiment of dipole coalescence are shown in Figure 3b,c. Water droplets are initially placed horizontally. Under the dielectric force, the water droplets deformed rapidly. Since the two droplets adhere to the electrodes with different forces, they move differently, and the angle between the droplets is no longer zero. Subsequently, the two water droplets produce dipole coalescence. The process is shown in Video S3 (Supporting Information). In the simulation, although the force of water droplets adhering to electrodes could not be simulated, the deformation of water droplets still moves them differently, making the angle between them diverge from zero. Finally, the dipole coalescence is completed.

Meanwhile, **Figure 4** shows the effects on electric field intensity and dielectric force. The effective parameters include water droplet size, position, and the dielectric constant of oil, in which the size and position of water droplets reflect the impact of the inhomogeneity of the dielectric constant mentioned in Equation (5). Figure 4a,b illustrates the electric field intensity and dielectric force variation around a single water droplet and two water droplets at different angles. The angle is marked in Figure S3 (Supporting Information). The water droplet simulated in Figure 4a is placed in the middle of the upper and lower electrodes so that the dielectric force generated is symmetric. When the position of the water droplet is not at the exact midpoint, the dielectric force is asymmetric, thus producing the oscillations in Figure S2 (Supporting Information). Figure 4b indicates that the dielectric force between the two droplets reaches the maximum when they are up and down. Figure 4c shows the effect of the dielectric constant, indicating the magnitude of the dielectric force generated on different types of oil with different dielectric constants. In Figure 4d, as the water droplets' center distance decreases, the electric field intensity between them increases. As shown in Figure 4e, when the distance between two water droplets is kept constant, the electric field intensity between them increases with the diameter of the water droplet. The variation of dielectric force with the diameter and center distance of water droplets is illustrated in Figure 4f. It is found that when two water droplets are close enough, there exists a considerable interaction between them, producing dipole coalescence.

The dynamic performance of water-in-oil emulsions under the electric field generated by the FR-TENG is analyzed in detail through simulations and experiments. Guidance is given for the subsequent dehydration performance experiments' variable selection.

2.3.2. Effects of Operating Conditions on the Dehydration Performance of the TED

Electric dehydration is relevant to the moisture content, continuous phase viscosity, electric field intensity, electric field uniformity, etc. **Figure 5** shows the three processes in the electric dehydration experiment. Before the dehydration, surfactant-stabilized water-in-oil emulsions with different initial moisture contents are prepared. Water bath heating changes the viscosity by controlling the temperature of the emulsion. During the dehydration, the upper dehydrated oil is sampled by a microsampler. The moisture titrator measures the moisture content of the sample every 5 min. Calculations of moisture content and

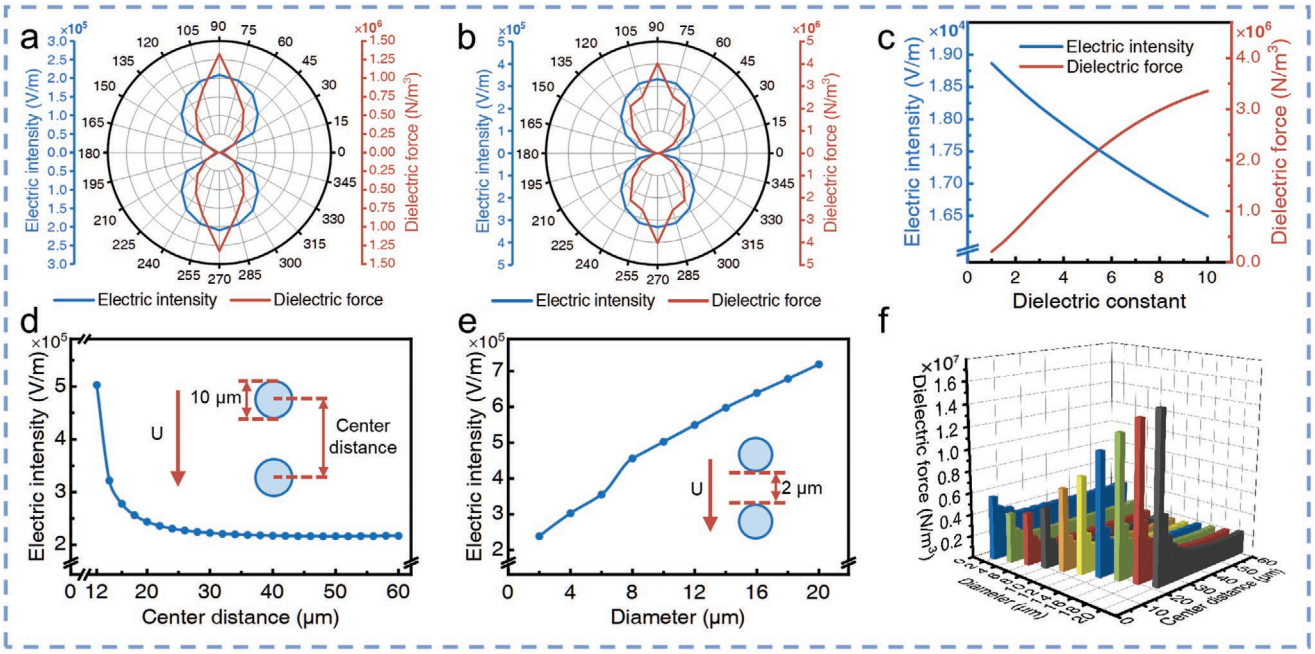

Figure 4. Simulation of electric field intensity and dielectric force in various water-in-oil emulsions. Variation for the electric field intensity and dielectric force a) around a water droplet and b) between two water droplets under different angles. c) The relationship of the dielectric constant with electric field intensity and dielectric force. d) The electric field intensity at different center distances between two water droplets. e) The electric field intensity with different diameters of two water droplets. f) The dielectric force with different diameters of water droplets at different center distances.

the dehydration rate are demonstrated in Note S2 (Supporting Information).

Two electrode structures, parallel electrode and wire–duct electrode, are used to compare the effects of electric field uniformity. The dimensions of the two electrode structures are marked in Figure S4 (Supporting Information). An acrylic polymethyl methacrylate (PMMA) vessel with an inner diameter of 42 mm is used as the container for both electrode structures. The electrode diameter is 35 mm for the parallel electrode, and the distance between electrodes is 20 mm. The distance between the wire surface and the duct is 20 mm for the wire–duct electrode.

First, the effect on the dehydration rate with or without an electric field is examined at room temperature. Emulsions with an initial moisture content of 10% are used. The dehydration rate is shown in Figure 5b. The electric field significantly enhances dehydration compared with gravity settling without the electric field. The dehydration is rapid in the earlier stage, while the dehydration gradually slows down in the later stage. Therefore, we defined the dehydration rate at 5 min as the dehydration speed and 60 min as the final dehydration rate. Then, experiments on the effect of electric field intensity on the dehydration rate of both electrode structures are carried out under the same conditions. As shown in Figure 5c, the dehydration speed and the final dehydration rate increase with the enhanced electric field intensity for both electrodes. The dehydration rate of the parallel electrode is 21.0–30.9% at 5 min with an average electric field intensity of 200–1000 V cm^{-1}. In comparison, the dehydration rate of the wire–duct electrode is 30.5–50.0%, implying that the dehydration speed of the wire–duct electrode is higher. At 60 min, the dehydration rate of the parallel electrode is 90.0–95.4%, while that of the wire–duct electrode is 84.0–86.4%. Compared with the wire–duct electrode, the parallel electrode has a relatively slower dehydration speed but a higher final dehydration rate, which is attributed to the difference in the electric field distribution. The electric field of the parallel electrode is more concentrated between the two electrodes, while the wire–duct electrode generates an electric field throughout the vessel. It is also why the wire–duct electrode has lower final moisture content. In the first stage of dehydration, although the parallel electrode has a more concentrated effect on the emulsion, the movement of separated oil and water is hindered by the electrode. In contrast, the wire–duct electrode does not, resulting in a higher dehydration speed.

The viscosity of emulsion decreases as temperature increases. To investigate the effect of viscosity, comparative experiments are conducted in a water bath at 50 °C versus the room temperature of 23 °C. Meanwhile, experiments are carried out at the average electric field intensity of 1000 V cm^{-1}. The effect of temperature on the dehydration rate is shown in Figure 5d. Both dehydration speed and the final dehydration rate were improved at 50 °C. As shown in Figure S5 (Supporting Information), under heating, the dehydration rate is 84.4% for the parallel electrode and 72.4% for the wire–duct electrode at 5 min. The dehydration speed is higher for the parallel electrode. At 50 °C, both the dehydration speed and the final dehydration rate with the parallel electrode were higher than those with the wire–duct electrode (97.2% for the parallel electrode and 93.1% for the wire–duct electrode at 60 min). This is because heating reduces the viscosity of the emulsion, thereby causing a much faster movement of dehydrated oil and water between the two electrodes, leading to the dehydration speed of the parallel electrode improving significantly.

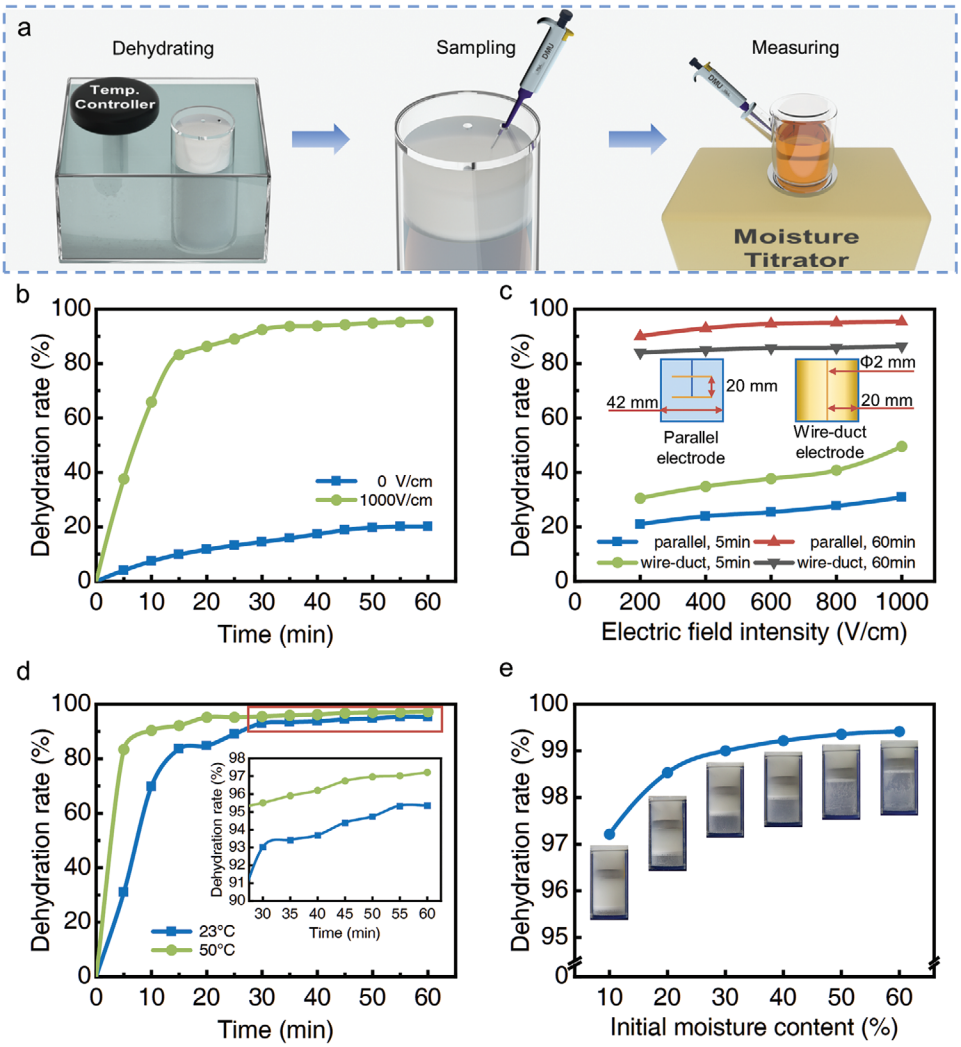

Figure 5. Effects of operating conditions on the performance of electric dehydration of the TED. a) Schematic diagram of the electric dehydration experiment process. b) Enhancement of the dehydration by the electric field powered by the FR-TENG compared with gravity settling. c) Effect on the dehydration rate with different average electric intensities for the two electrode structures at 5 and 60 min. d) Promotion of dehydration by increasing the temperature of the emulsion. e) Variation of the final dehydration rate with different initial moisture content.

Experiments with different initial moisture contents are carried out under the condition of the parallel electrode at 50 °C with an average electric field intensity of 1000 V cm^{-1}. In Figure 5e, photos show the presence of dehydrated water-in-oil emulsions with different initial moisture contents. Simultaneously, Figure 5e demonstrates that the final dehydration rate increases with the increase of the initial moisture content. The highest final dehydration rate is 99.41%, with an initial moisture content of 60%.

The number of water droplets in the water-in-oil emulsion increases as the initial moisture content rises, and their spacing decreases, making it easier to induce water droplets' oscillation coalescence. Simultaneously, since the center distance between water droplets is small, the dielectric force between them is stronger, resulting in an easier induced dipole coalescence. Figure S6 (Supporting Information) illustrates the variation of emulsion water content with time for different initial moisture contents. As shown in Figure S7 (Supporting Information), the dehydration speed increases and decreases with the increase of initial moisture content, owing to the dehydration rate calculated by dividing the initial moisture content. In addition, experiments with various temperatures, electrode structures, initial moisture contents, and average electric intensities are completed. The results are shown in Figures S8 and S9 (Supporting Information). Overall, the electric field is the one that most promotes dehydration compared to the other conditions. Video S4 (Supporting Information) demonstrates the microscopic dynamics of the emulsion during dehydration. It can be observed that the TED is very efficient in dehydration.

The working moisture content of a traditional electric dehydrator is usually below 20%. For the traditional electric dehydrator with a pulsed electric field and insulated electrodes, the applicable moisture content is nearly 40%. The range of moisture content that the TED can dehydrate in the experiment covers almost the whole moisture range of water-in-oil emulsions because the electrical characteristics of the FR-TENG are fundamentally different from those of traditional high-voltage power supplies.

2.4. Demonstration of a Wind-Driven TED

A TENG already has successful applications for harvesting environmental energy, such as wind speed sensor,[53] hydrological monitoring system,[54] smart home/city,[55] wheel monitoring,[56] and intelligent transportation system,[57] making a wind-driven TED possible. As shown in **Figure 6**a, the TED harvests environmental energy through a windmill that converts wind energy into mechanical energy and drives the FR-TENG to rotate. The FR-TENG generates high-voltage output electricity, eventually driving the electric dehydration. As shown in Figure S10 (Supporting Information), a shaft delivers the torque of the windmill to the rotor of the FR-TENG. As there is a resistance torque between the rotor and the stator of the FR-TENG, the torque generated on the windmill should be bigger than the resistance torque. On the other hand, the rotational inertia of the rotor determines the required torque for rotation. In this sense, a rotor 3D-printed with foamed polylactic acid (PLA) significantly reduces the rotational inertia. This is due to the PMMA density of 1.2 g cm^{-3}, and the foamed PLA density of only 0.54 g cm^{-3}, as well as the structural optimization.

The rotors made of acrylic and foamed PLA are pulled uniformly using a tensiometer at various gap distances to measure the starting torque. The results are shown in Figure 6b. The increase in gap distance significantly reduces the torque required for initializing the rotation. The photo of the lab bench is shown in Figure 6c. The airflow generated by the fan simulates the natural wind with a certain wind speed. The wind speed is measured precisely by an anemometer in front of the windmill.

As shown in Video S5 (Supporting Information), the FR-TENG with a 3D-printed rotor is driven by wind energy. The FR-TENG with a 17 mm gap distance rotates continuously and completes the dehydration. A photograph of the emulsion in dehydration is shown in Figure 6d. The wind speed is about 6 m s^{-1}, equivalent to the class 4 wind. There is still room for optimizing the interactions between the wind turbine and the FR-TENG. By optimizing the windmill for the FR-TENG, possibly lower-speed winds can drive the TED.

3. Conclusions

The present work proposed a self-powered and efficient triboelectric dehydrator for separating water-in-oil emulsions with ultrahigh moisture content. The triboelectric dehydrator consists of parallel electrodes connecting to the FR-TENG. A high-voltage electric field is formed between the parallel electrodes placed in the emulsion when the TENG is driven by mechanical energy. To understand the dynamic performance of water droplets in oil under the high-voltage electric field, the laminar flow model, the level-set two-phase flow model, and the electrostatic model are coupled to simulate the interactions between water droplets in oil under the electric field. It is found that the dielectric force generated by TED promotes the coalescence of water droplets through dipole coalescence and oscillation coalescence. Moreover, the effects of continuous phase viscosity, electric field intensity, electric field uniformity, and initial moisture content on the dehydration performance of the TED are experimentally investigated. The results show that the TED can dehydrate water-in-oil emulsions with the moisture content from 10% to 60%. In particular, the dehydration rate of the TED reaches 99.41% even when the initial moisture content is 60% which is near the phase inversion concentration of the emulsions. This indicates that the dehydrating capability of the TED is outstanding under various conditions, demonstrating advantageous efficiency and stability,

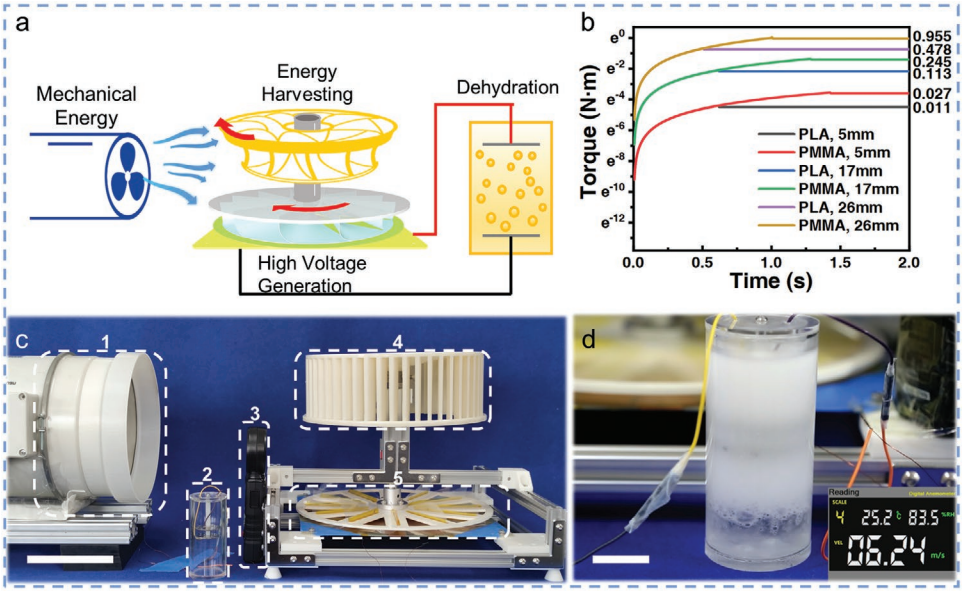

Figure 6. Demonstration of the wind-driven TED for separating water-in-oil emulsions. a) A schematic diagram of the wind-driven TED lab bench and energy cycle. b) The torque variation in driving the FR-TENG at gap distances of 5, 17, and 26 mm. c) A lab bench photo of the wind-driven TED. 1 to 5 represents the fan, the vessel of the TED, the anemometer, the windmill, and the FR-TENG, respectively (scale bar: 10 cm). d) Photograph of the dehydrated emulsion with the power supply of harvesting wind energy (scale bar: 2 cm).

especially for ultrahigh moisture content in water-in-oil emulsions. In addition, the TED driven by wind energy is successfully demonstrated to dehydrate the water-in-oil emulsions. The present work has proved that TED has great potential application for separating oil–water emulsions.

4. Experimental Section

Measurement of the Electrical Characteristics of an FR-TENG: A Keithley 6514 electrometer was used as a power measurement device with an internal resistance of ≈200 TΩ. The voltage or current measurements can be selected by switching between the different ranges. When measuring voltage, the Keithley 6514 electrometer was connected in series with a PINTECH HVP-40 high-voltage probe with an impedance of 1 GΩ because the voltage was out of range.

Measurement of the Water Cut in Oil: A Byes-8 Karl Fischer moisture titrator was used for the measurement of moisture content. The device uses the Karl Fischer Coulomb titration method with a measurement range from 3 µg to 100 mg, a sensitivity of 0.1 µg, and an accuracy from 3 µg to 1 mg ± 2 µg.

Demo Capture and Wind Speed Measurement: The camera used for the shooting was a CANON EOS 5D Mark III, and the microscopic effects were taken with a CCD microscope. The wind speed in the demo was measured with an Aicevoos H6 anemometer.

Structural Design of the FR-TENG and Wind-Driven TED: The FR-TENG was composed of two parts: a stator and a rotor. For the stator, i) the TENG stator (300 mm × 300 mm × 2 mm) was made of an FR-4 board with a grid-shaped copper electrode coated on the surface. The positive and negative electrodes were alternately arranged, with a 3 mm space between them. ii) A nylon layer with a thickness of 50 µm was tautly applied to the surface of the TENG stator using textured paper tape. In the rotor, i) a laser cutter was used to cut an acrylic sheet that was 4 mm thick. It made a disk that had an outside diameter of 320 mm and an inside diameter of 20 mm. The hole in the center of the substrate was for attaching to the shaft through the flange. ii) By the laser cutter, 12 radially arranged slots of 1 mm width and 107.5 mm length were cut into the disk. iii) The PVC film with a thickness of 100 µm was inserted in the slots and held in place by Kapton tape. Based on the FR-TENG, the wind-driven TED replaced the rotor and added a windmill. i) The rotor was made of 3D-printed foamed PLA material with a thickness of 4 mm and an outside diameter of 310 mm. A total of 12 radially arranged slots were also printed on the rotor. ii) A hollow design was used at a distance of 15 mm away from the two slots and the outer diameter. The windmill was constructed of plastic, with an outside diameter of 280 mm, a height of 135 mm, and a total of 48 blades.

Supporting Information

Supporting Information is available from the Wiley Online Library or from the author.

Acknowledgements

F.L., X.W., and J.H. contributed equally to this work. The work was supported by the National Key R & D Project from Minister of Science and Technology (Project No. 2021YFA1201604), the National Natural Science Foundation of China (Grant Nos. 51879022, 51979045, 52101400, 52101382, and 52101345), Dalian Outstanding Young Scientific and Technological Talents Project (Project No. 2021RJ11).

Conflict of Interest

The authors declare no conflict of interest.

Data Availability Statement

The data that support the findings of this study are available from the corresponding author upon reasonable request.

Keywords

triboelectric dehydrator, triboelectric nanogenerator, self-powered, water-in-oil emulsions

Received: February 7, 2022
Revised: March 9, 2022
Published online:

[1] I. C. Ossai, A. Ahmed, A. Hassan, F. S. Hamid, *Environ. Technol. Innovation* **2020**, *17*, 100526.
[2] M. D. Soares, C. E. P. Teixeira, L. E. A. Bezerra, S. V. Paiva, T. C. L. Tavares, T. M. Garcia, J. T. de Araujo, C. C. Campos, S. M. C. Ferreira, H. Matthews-Cascon, A. Frota, T. C. F. Mont'Alverne, S. T. Silva, E. F. Rabelo, C. X. Barroso, J. E. P. de Freitas, M. de Melo, R. P. D. Campelo, C. S. de Santana, P. B. D. Carneiro, A. J. Meirelles, B. A. Santos, A. H. B. de Oliveira, P. Horta, R. M. Cavalcante, *Mar. Policy* **2020**, *115*, 103879.
[3] N. M. Reid, D. A. Proestou, B. W. Clark, W. C. Warren, J. K. Colbourne, J. R. Shaw, S. I. Karchner, M. E. Hahn, D. Nacci, M. F. Oleksiak, D. L. Crawford, A. Whitehead, *Science* **2016**, *354*, 1305.
[4] F. Brette, B. Machado, C. Cros, J. P. Incardona, N. L. Scholz, B. A. Block, *Science* **2014**, *343*, 772.
[5] B. Q. Huynh, L. H. Kwong, M. V. Kiang, E. T. Chin, A. M. Mohareb, A. O. Jumaan, S. Basu, P. Geldsetzer, F. M. Karaki, D. H. Rehkopf, *Nat. Sustainability* **2021**, *4*, 1084.
[6] J. Saththasivam, K. Loganathan, S. Sarp, *Chemosphere* **2016**, *144*, 671.
[7] F. C. P. Rocha e Silva, N. M. P. Rocha e Silva, I. A. da Silva, P. P. Ferreira Brasileiro, J. M. Luna, R. D. Rufino, V. A. Santos, L. A. Sarubbo, *J. Water Process Eng.* **2018**, *23*, 45.
[8] M. Liu, J. Chen, X. Cai, Y. Han, S. Xiong, *Chin. J. Chem. Eng.* **2018**, *26*, 60.
[9] X. Yang, Z. Wang, L. Shao, *J. Membr. Sci.* **2018**, *549*, 67.
[10] S. Rasouli, N. Rezaei, H. Hamedi, S. Zendehboudi, X. Duan, *Mater. Des.* **2021**, *204*, 109599.
[11] I. Kailey, *Energy Fuels* **2016**, *30*, 9233.
[12] O. A. Adeyanju, L. O. Oyekunle, *Egypt. J. Pet.* **2019**, *28*, 349.
[13] D. Wang, D. Yang, C. Huang, Y. Huang, D. Yang, H. Zhang, Q. Liu, T. Tang, M. Gamal El-Din, T. Kemppi, B. Perdicakis, H. Zeng, *Fuel* **2021**, *286*, 119390.
[14] W.-T. Kwon, K. Park, S. D. Han, S. M. Yoon, J. Y. Kim, W. Bae, Y. W. Rhee, *J. Ind. Eng. Chem.* **2010**, *16*, 684.
[15] C. Guo, L. He, *J. Electrost.* **2014**, *72*, 470.
[16] B. Li, V. Vivacqua, M. Ghadiri, Z. Sun, Z. Wang, X. Li, *Chem. Eng. Res. Des.* **2017**, *127*, 180.
[17] Z. L. Wang, *ACS Nano* **2013**, *7*, 9533.
[18] Z. L. Wang, J. Chen, L. Lin, *Energy Environ. Sci.* **2015**, *8*, 2250.
[19] J. Chen, Y. Huang, N. Zhang, H. Zou, R. Liu, C. Tao, X. Fan, Z. L. Wang, *Nat. Energy* **2016**, *1*, 16138.
[20] H. Guo, J. Chen, L. Wang, A. C. Wang, Y. Li, C. An, J.-H. He, C. Hu, V. K. S. Hsiao, Z. L. Wang, *Nat. Sustainability* **2020**, *4*, 147.
[21] L. Long, W. Liu, Z. Wang, W. He, G. Li, Q. Tang, H. Guo, X. Pu, Y. Liu, C. Hu, *Nat. Commun.* **2021**, *12*, 4689.
[22] Y. X. Shi, F. Wang, J. W. Tian, S. Y. Li, E. G. Fu, J. H. Nie, R. Lei, Y. F. Ding, X. Y. Chen, Z. L. Wang, *Sci. Adv.* **2021**, *7*, eabe2943.

[23] X. Pu, M. M. Liu, X. Y. Chen, J. M. Sun, C. H. Du, Y. Zhang, J. Y. Zhai, W. G. Hu, Z. L. Wang, *Sci. Adv.* **2017**, *3*, e1700015.
[24] J. Nie, X. Chen, Z. L. Wang, *Adv. Funct. Mater.* **2019**, *29*, 1806351.
[25] W. Ding, J. Zhou, J. Cheng, Z. Wang, H. Guo, C. Wu, S. Xu, Z. Wu, X. Xie, Z. L. Wang, *Adv. Energy Mater.* **2019**, *9*, 1901320.
[26] Z. Wang, Y. Shi, F. Liu, H. Wang, X. Liu, R. Sun, Y. Lu, L. Ji, Z. L. Wang, J. Cheng, *Nano Energy* **2020**, *74*, 104910.
[27] J. Cheng, W. Ding, Y. Zi, Y. Lu, L. Ji, F. Liu, C. Wu, Z. L. Wang, *Nat. Commun.* **2018**, *9*, 3733.
[28] Y. Liu, B. Chen, W. Li, L. Zu, W. Tang, Z. L. Wang, *Adv. Funct. Mater.* **2021**, *31*, 2104770.
[29] W. Sun, B. Li, F. Zhang, C. Fang, Y. Lu, X. Gao, C. Cao, G. Chen, C. Zhang, Z. L. Wang, *Nano Energy* **2021**, *85*, 106012.
[30] J. Yu, X. Wei, Y. Guo, Z. Zhang, P. Rui, Y. Zhao, W. Zhang, S. Shi, P. Wang, *Lab Chip* **2021**, *21*, 284.
[31] L. Liu, L. Zhou, D. Liu, W. Yuan, S. Chen, H. Li, Z. Bian, J. Wang, Z. L. Wang, *ACS Nano* **2021**, *15*, 5478.
[32] H. Huo, F. Liu, Y. Luo, Q. Gu, Y. Liu, Z. Wang, R. Chen, L. Ji, Y. Lu, R. Yao, J. Cheng, *Nano Energy* **2020**, *67*, 104150.
[33] C. Li, Y. Yin, B. Wang, T. Zhou, J. Wang, J. Luo, W. Tang, R. Cao, Z. Yuan, N. Li, X. Du, C. Wang, S. Zhao, Y. Liu, Z. L. Wang, *ACS Nano* **2017**, *11*, 10439.
[34] R. Lei, Y. Shi, Y. Ding, J. Nie, S. Li, F. Wang, H. Zhai, X. Chen, Z. L. Wang, *Energy Environ. Sci.* **2020**, *13*, 2178.
[35] J. S. Eow, M. Ghadiri, *Chem. Eng. J.* **2002**, *85*, 357.
[36] V. Vivacqua, S. Mhatre, M. Ghadiri, A. M. Abdullah, A. Hassanpour, M. J. Al-Marri, B. Azzopardi, B. Hewakandamby, B. Kermani, *Chem. Eng. Res. Des.* **2015**, *104*, 658.
[37] B. Li, Z. Sun, Z. Wang, Y. Jin, Y. Fan, *J. Electrost.* **2016**, *80*, 22.
[38] Y. Zhou, Z. Wang, Z. Sun, *Chem. Eng. Res. Des.* **2022**, *177*, 65.
[39] D. Yang, Y. Feng, B. Wang, Y. Liu, Y. Zheng, X. Sun, J. Peng, M. Feng, D. Wang, *Nano Energy* **2021**, *90*, 106641.
[40] Y. Peng, B. Yu, X. Zhang, H. Gong, Y. Liu, *Chem. Eng. Process.* **2020**, *148*, 107803.
[41] C. Lesaint, G. Berg, L. Lundgaard, M. G. Ese, *IEEE Trans. Dielectr. Electr. Insul.* **2016**, *23*, 2015.
[42] C. Lesaint, W. R. Glomm, L. E. Lundgaard, J. Sjöblom, *Colloids Surf., A* **2009**, *352*, 63.
[43] Y. Zhang, Y. Liu, R. Ji, *Colloids Surf., A* **2011**, *373*, 130.
[44] H. Lu, S. Wu, Z. Miao, X. Xu, Y. Liu, Z. Wang, H. Wang, Q. Yang, *Chem. Eng. Sci.* **2021**, *241*, 116680.
[45] B. Li, Y. Fan, Z. Sun, Z. Wang, L. Zhu, *Powder Technol.* **2017**, *316*, 338.
[46] A. H. Selker, C. A. SleicherJr, *Can. J. Chem. Eng.* **1965**, *43*, 298.
[47] E. Dickinson, *J. Colloid Interface Sci.* **1982**, *87*, 416.
[48] A. Perazzo, V. Preziosi, S. Guido, *Adv. Colloid Interface Sci.* **2015**, *222*, 581.
[49] Y. Mori, M. Tanigaki, N. Maehara, *J. Chem. Eng. Jpn.* **1994**, *27*, 340.
[50] O. Lastow, W. Balachandran, *J. Electrost.* **2006**, *64*, 850.
[51] H. H. Woodson, J. R. Melcher, *Electromechanical Dynamics, Part II: Fields, Forces, and Motion*, John Wiley and Sons, Inc, New York, NY **1968**.
[52] X. Zhao, X. Lu, Q. Zheng, L. Fang, L. Zheng, X. Chen, Z. L. Wang, *Nano Energy* **2021**, *87*, 106191.
[53] P. Wang, L. Pan, J. Wang, M. Xu, G. Dai, H. Zou, K. Dong, Z. L. Wang, *ACS Nano* **2018**, *12*, 9433.
[54] P. Rui, W. Zhang, Y. Zhong, X. Wei, Y. Guo, S. Shi, Y. Liao, J. Cheng, P. Wang, *Nano Energy* **2020**, *74*, 104937.
[55] Y. Zhong, H. Zhao, Y. Guo, P. Rui, S. Shi, W. Zhang, Y. Liao, P. Wang, Z. L. Wang, *Adv. Mater. Technol.* **2019**, *4*, 1900741.
[56] L. Jin, S. L. Zhang, S. Xu, H. Guo, W. Yang, Z. L. Wang, *Adv. Mater. Technol.* **2021**, *6*, 2000918.
[57] L. Jin, B. Zhang, L. Zhang, W. Yang, *Nano Energy* **2019**, *66*, 104086.